Chemically-selective imaging of brain structures with CARS microscopy

Conor L. Evans[1§], Xiaoyin Xu[2§], Santosh Kesari[3], X. Sunney Xie[1], Stephen T.C. Wong[4], and Geoffrey S. Young[2, 5*]

[1]*Department of Chemistry and Chemical Biology, Harvard University, Cambridge, MA*
[2]*Functional and Molecular Imaging Center, Department of Radiology, Brigham and Women's Hospital, Boston, MA*
[3] *Dana-Farber Cancer Institute and Department of Neurology, Brigham and Women's Hospital, Boston, M,*
[4]*Department of Radiology, Methodist Hospital-Weill Cornell Medical College and Center for Bioinformatics, The Methodist Hospital Research Institute, Houston, TX*
[5]*Neuroradiology Section, Department of Radiology, Brigham and Women's Hospital, Boston, MA, USA*
* Corresponding Author: gsyoung@partners.org

Abstract: We demonstrate the use of coherent anti-Stokes Raman scattering (CARS) microscopy to image brain structure and pathology *ex vivo*. Although non-invasive clinical brain imaging with CT, MRI and PET has transformed the diagnosis of neurologic disease, definitive pre-operative distinction of neoplastic and benign pathologies remains elusive. Definitive diagnosis still requires brain biopsy in a significant number of cases. CARS microscopy, a nonlinear, vibrationally-sensitive technique, is capable of high-sensitivity chemically-selective three-dimensional imaging without exogenous labeling agents. Like MRI, CARS can be tuned to provide a wide variety of possible tissue contrasts, but with sub-cellular spatial resolution and near real time temporal resolution. These attributes make CARS an ideal technique for fast, minimally invasive, non-destructive, molecularly specific intraoperative optical diagnosis of brain lesions. This promises significant clinical benefit to neurosurgical patients by providing definitive diagnosis of neoplasia prior to tissue biopsy or resection. CARS imaging can augment the diagnostic accuracy of traditional frozen section histopathology in needle biopsy and dynamically define the margins of tumor resection during brain surgery. This report illustrates the feasibility of *in vivo* CARS vibrational histology as a clinical tool for neuropathological diagnosis by demonstrating the use of CARS microscopy in identifying normal brain structures and primary glioma in fresh unfixed and unstained *ex vivo* brain tissue.

OCIS codes: (300.6230) Spectroscopy, coherent anti-Stokes Raman scattering; (300.6450) Spectroscopy, Raman; (170.6510) Spectroscopy, tissue diagnostics; (170.4580) Optical diagnostics for medicine; (170.4730) Optical pathology; (180.6900) Three-dimensional microscopy

References and links

1. D. D. Langleben, and G. M. Segall, "PET in differentiation of recurrent brain tumor from radiation injury," J. Nucl. Med. **41**, 1861-1867 (2000).
2. M. C. Preul, R. Leblanc, Z. Caramanos, R. Kasrai, S. Narayanan, and D. L. Arnold, "Magnetic resonance spectroscopy guided brain tumor resection: differentiation between recurrent glioma and radiation change in two diagnostically difficult cases," Can. J. Neurol. Sci. **25**, 13-22 (1998).
3. Y. Ge, M. Law, and R. I. Grossman, "Applications of diffusion tensor MR imaging in multiple sclerosis," Ann. N Y Acad. Sci. **1064**, 202-219 (2005).
4. D. Goldberg-Zimring, A. U. Mewes, M. Maddah, and S. K. Warfield, "Diffusion tensor magnetic resonance imaging in multiple sclerosis," J. Neuroimaging **15**, 68S-81S (2005).

5. W. R. Zipfel, R. M. Williams, R. Christie, A. Y. Nikitin, B. T. Hyman, and W. W. Webb, "Live tissue intrinsic emission microscopy using multiphoton-excited native fluorescence and second harmonic generation," Proc. Natl. Acad. Sci. U S A **100**, 7075-7080 (2003).
6. P. J. Campagnola, A. C. Millard, M. Terasaki, P. E. Hoppe, C. J. Malone, and W. A. Mohler, "Three-dimensional high-resolution second-harmonic generation imaging of endogenous structural proteins in biological tissues," Biophys. J. **81**, 493-508 (2002).
7. W. R. Zipfel, R. M. Williams, and W. W. Webb, "Nonlinear magic: multiphoton microscopy in the biosciences," Nat. Biotechnol. **21**, 1369-1377 (2003).
8. G. J. Tearney, M. E. Brezinski, B. E. Bouma, S. A. Boppart, C. Pitris, J. F. Southern, and J. G. Fujimoto, "In Vivo Endoscopic Optical Biopsy with Optical Coherence Tomography," Am. J. of Physiol. **268**, H802 (1995).
9. J. G. Fujimoto, "Optical coherence tomography - a review of the principles and contemporary uses in retinal investigation," Nat. Biotechnol. **21**, 1361--1367 (2003).
10. J. X. Cheng, and X. S. Xie, "Coherent anti-Stokes Raman scattering microscopy: instrumentation, theory, and applications," J. Phys. Chem. B **108**, 827-840 (2004).
11. F. Ganikhanov, C. L. Evans, B. G. Saar, and X. S. Xie, "High sensitivity vibrational imaging with frequency modulation coherent anti-Stokes Raman scattering (FM CARS) microscopy," Opt. Lett. **31**, 1872-1874 (2006).
12. C. L. Evans, E. O. Potma, M. Puoris'haag, D. Côté, C. P. Lin, and X. S. Xie, "Chemical imaging of tissue in vivo with video-rate coherent anti-Stokes Raman scattering microscopy," Proc. Natl. Acad. Sci. U S A **102**, 16807-16812 (2005).
13. E. Potma, W. P. de Boeij, P. J. van Haastert, and D. A. Wiersma, "Real-time visualization of intracellular hydrodynamics in single living cells," Proc. Natl. Acad. Sci. U S A **98**, 1577-1582 (2001).
14. X. Nan, E. O. Potma, and X. S. Xie, "Nonperturbative chemical imaging of organelle transport in living cells with coherent anti-stokes Raman scattering microscopy," Biophys. J. **91**, 728-735 (2006).
15. F. Ganikhanov, S. Carrasco, X. Sunney Xie, M. Katz, W. Seitz, and D. Kopf, "Broadly tunable dual-wavelength light source for coherent anti-Stokes Raman scattering microscopy," Opt. Lett. **31**, 1292-1294 (2006).
16. H. Wang, Y. Fu, P. Zickmund, R. Shi, and J. X. Cheng, "Coherent anti-stokes Raman scattering imaging of axonal myelin in live spinal tissues," Biophys. J. **89**, 581-591 (2005).
17. F. Helmchen, and W. Denk, "Deep tissue two-photon microscopy," Nature **200**, 5 (2002).
18. M. Rueckel, J. A. Mack-Bucher, and W. Denk, "Adaptive wavefront correction in two-photon microscopy using coherence-gated wavefront sensing," Proc. Natl. Acad. Sci. U S A **103**, 17137 (2006).
19. P. Marsh, D. Burns, and J. Girkin, "Practical implementation of adaptive optics in multiphoton microscopy," Opt. Express **11**, 1123--1130 (2003).
20. M. Müller, and J. M. Schins, "Imaging the thermodynamics state of lipid membranes with multiplex CARS microscopy," J. Phys. Chem. B **106**, 3715-3723 (2002).
21. J. X. Cheng, A. Volkmer, L. D. Book, and X. S. Xie, "Multiplex coherent anti-Stokes Raman scattering microspectroscopy and study of lipid vesicles," J. Phys. Chem. B **106**, 8493-8498 (2002).
22. E. O. Potma, C. Evans, X. S. Xie, R. J. Jones, and J. Ye, "Picosecond-pulse amplification with an external passive optical cavity," Opt. Lett. **28**, 1835-1837 (2003).
23. A. Mizuno, T. Hayashi, K. Tashibu, S. Maraishi, K. Kawauchi, and Y. Ozaki, "Near-infrared FT-Raman spectra of the rat brain tissues," Neurosci. Lett. **141**, 47-52 (1992).
24. C. W. Ong, Z. X. Shen, Y. He, T. Lee, and S. H. Tang, "Raman Microspectroscopy of the brain tissues in the substantia nigra and MPRP-induced Parkinson's disease," J. Raman Spectrosc. **30**, 91-96 (1999).
25. S. C. Gebhart, W. C. Lin, and A. Mahadevan-Jansen, "In vitro determination of normal and neoplastic human brain tissue optical properties using inverse adding-doubling," Phys. Med. Biol. **51**, 2011-2027 (2006).
26. E. O. Potma, C. L. Evans, and X. S. Xie, "Heterodyne coherent anti-Stokes Raman scattering (CARS) imaging," Opt Lett **31**, 241-243 (2006).
27. A. Mehta, J. Jung, B. Flusberg, and M. Schnitzer, "Fiber optic in vivo imaging in the mammalian nervous system," Curr. Opin. Neurobiol. **14**, 11 (2004).
28. B. A. Flusberg, J. C. Jung, E. D. Cocker, E. P. Anderson, and M. J. Schnitzer, "In vivo brain imaging using a portable 3.9 gram two-photon fluorescence microendoscope," Opt. Lett. **30**, 3 (2005).
29. F. Légaré, C. L. Evans, F. Ganikhanov, and X. S. Xie, "Towards CARS Endoscopy," Opt. Express **14**, 4427-4432 (2006).

1. Introduction

Diverse neuropathologies including demyelination (multiple sclerosis, acute disseminated encephalomyelitis), ichemia, viral infection (progressive multifocal leukoencephalopathy), bacterial or fungal abscess, granulomatous disease (sarcoidosis), and primary CNS lymphoma may be difficult to distinguish from primary brain tumor (glioma) by MRI and CT and often require surgical brain biopsy for diagnosis. Similarly, in patients with known brain tumors treated by radiotherapy, it is often difficult to differentiate between radiation injury and

recurrent malignancy on MRI [1, 2]. The risks of brain biopsy are acceptable for patients with new or recurrent glioma because definitive therapy often includes surgical resection prior to radiation and chemotherapy. However, patients with radiation necrosis, demyelination or any of the other diagnoses mentioned do not require surgical resection, and so the morbidity and mortality of brain biopsy is a significant contributor to the injury caused by the disease itself. Although advanced imaging techniques such as MRI diffusion weighted imaging, diffusion tensor imaging, perfusion imaging, permeability imaging and spectroscopy can contribute to the differential diagnosis of masses in the brain, in many cases these techniques are not definitive enough to substitute for pathologic tissue diagnosis [3, 4]. In these patients it would be desirable to exclude glioma without resection of brain tissue, in order to minimize the morbidity of neurosurgical biopsy.

Clearly, a technique that could differentiate the aforementioned non-neoplastic conditions and CNS lymphoma from glioma prior to resection of brain tissue would be very desirable. Definitive diagnosis by MRI or PET, however, seems unlikely in the near future. The lower spatial resolution and tissue contrast of these techniques remain inadequate substitutes for the cellular and tissue scale morphologic information that has made microscopic histopathology the diagnostic gold standard for over a century. In the absence of a completely non-invasive pre-operative imaging diagnosis, it would be ideal to diagnose brain lesions *in situ* through a small burr hole in the skull before deciding whether to perform a larger craniotomy or to resect tissue. To be useful, such a method would need to produce cellular and tissue level images of the intact brain in near real time, with minimal or no tissue damage. A technique that could produce such images without relying on potentially toxic exogenous labeling agents such as fluorescent or heavy metal stains would be even more useful since few labeling agents have been proven safe enough for *in vivo* human use.

Optical techniques that utilize the intrinsic chemical composition of a specimen to produce microscopic images with different chemical 'weightings' offer one promising approach. Endogenous multiphoton fluorescence imaging techniques have found a number of applications in brain imaging [5], but the small number of naturally fluorescent compounds limits their general use. Structurally-sensitive imaging modalities such as second harmonic generation microscopy have been used in biomedical studies [6, 7], but are limited only to select proteins. Optical coherence tomography, a powerful approach that has found extensive use in biomedical imaging [8, 9], derives its contrast from changes in the index of refraction of a specimen, which are not always molecularly-specific.

Coherent anti-Stokes Raman scattering (CARS) microscopy [10] is a highly sensitive [11] vibrationally-selective imaging modality capable of rapid *in vivo* molecular imaging [12]. Because the contrast in CARS microscopy arises from the intrinsic molecular vibrations in a specimen, CARS is analogous to MRI in its ability to produce images with a variety of chemically selective contrasts. While it lacks the tissue penetration of MRI, CARS microscopy is capable of providing molecular information with sub-micron spatial resolution, allowing the production of images depicting intact tissue and cellular architecture *in situ.* CARS images thus offer information that is complementary to traditional histopathology techniques and may contain adequate information to substitute for traditional frozen section light microscopy in some intra-operative applications. In CARS, a pump beam, at frequency ω_p, and a Stokes beam, at frequency ω_s, interact with a sample through a four wave mixing process. When the beat frequency ($\omega_p - \omega_s$) is tuned to match the frequency of a Raman active molecular vibration, resonant molecules are coherently driven with the excitation fields, resulting in the generation of a strong "anti-Stokes" signal at $\omega_{as} = 2\omega_p - \omega_s$. Due to the nonlinear nature of the CARS process, the anti-Stokes signal is only generated at a small focal spot that can be scanned in space, allowing the acquisition of high-resolution, three-dimensional image volumes. In thick, turbid tissue such as brain matter, a large percentage of the CARS signal is redirected through multiple scattering events into the backwards (epi) direction, and can be easily collected by a large-area point detector [12].

With a signal strength that is orders of magnitude greater than conventional Raman scattering, and spatial resolutions far better than infrared imaging, CARS microscopy has

been used to image DNA and protein concentrations [10], water distributions [13], and lipid transport in living cells [14]. CARS microscopy has recently been used to image tissue in a living organism at the video-rate [12], allowing for real-time, chemically-selective imaging *in vivo*. Here we report the use of CARS microscopy to image fresh unfixed normal and diseased brain tissue, revealing microscopic scale structures in the brain without the need for tissue staining.

2. Materials and methods

2.1 Laser source

In order to minimize sample photodamage, the light source was operated in the near infrared. The laser system (Fig. 1) consisted of an optical parametric oscillator (OPO) [15] (Levante Emerald, APE-Berlin) pumped by a frequency-doubled Nd:YVO$_4$ modelocked laser. The pump laser (High-Q Laser Production GmbH) generates a 7 ps, 76 MHz pulse train of 1064 nm laser light with over 10 W of output power. An external temperature-controlled frequency doubler converts a large fraction of the fundamental, generating 4.5 W of 5 ps-duration 532 nm output. The OPO utilizes a temperature tuned, noncritically phase-matched LBO (LiB$_3$O$_5$) crystal for parametric downconversion. While the temperature of the crystal was set to generate near infrared signal and idler wavelengths, precise wavelength tuning was accomplished through the use of a stacked Lyot filter positioned in the cavity at Brewster's angle. By using a noncritically phased matched crystal for optical parametric generation, the signal and idler wavelengths exit the laser cavity in a collinear fashion, with pulse trains automatically overlapped in time. The OPO can be continuously tuned over a wide wavelength range from 670 nm to 980 nm for the signal and between 1130 nm and 1450 nm for the idler output. This flexible light source was operated in two configurations to maximize either the total detected CARS signal or penetration depth. To maximize the penetration depth, the signal and idler pulse trains, already collinear and overlapped in time, were used as the pump and Stokes wavelengths, respectively, for the CARS process [Fig. 1(a)]. In a second configuration used to maximize the detected CARS signal, the signal beam was separated from the idler and combined with a portion of the remaining 1064 nm pulse train. Anti-Stokes light generated using this wavelength combination backscattered more efficiently due to its shorter wavelength and was detected at higher quantum efficiencies by a photomultiplier tube. The signal and 1064 nm pulse trains were overlapped in time using a delay stage and sent collinearly into the microscope [Fig. 1(b)].

2.2 Laser scanning microscope

The CARS images were acquired using a modified commercial beam-scanning microscope (Fig. 1(c), Olympus IX71/FV300). Typical commercial microscopes have poor throughput in the near infrared, with less than 1% total throughput at wavelengths near 1250 nm. In order to optimize the microscope throughput, several modifications were made. The stock galvanometric scanning mirrors were replaced with silver galvanometric mirrors and the tube lens was replaced with an Olympus-modified MgF$_2$ coated lens for high throughput throughout the visible and near infrared spectrum. As CARS is a nonlinear process, confocal detectors are not necessary for imaging. The scanning confocal dichroic, therefore, was replaced by a silver mirror to ensure high reflectivity throughout the visible and NIR.

A 20X 0.75NA air objective (UPlanSApo UIS2, Olympus) was used for all imaging. This objective had excellent transmission properties and very low axial and lateral chromatic aberrations, allowing for large CARS signals with a full field of view. The anti-Stokes signal was separated from the pump and Stokes beams by a short-wave pass dichroic (750dcxr for signal and 1064 nm, z850rdc-xr for signal and idler, Chroma Technologies) and isolated using a stack of three 670 nm bandpass filters (30 nm bandwidth 42-3793, Coherent-Ealing) when 1064 nm was used as the Stokes wavelength, or a single 750 nm centered filter (hq750/210m, Chroma Technologies) when the signal and idler combination was used. A red-sensitive photomultiplier tube (R3896, Hammamatsu) was used as a nondescanned epi-detector. A

motorized, calibrated scanning stage was used to translate the sample to build up large tissue mosaics.
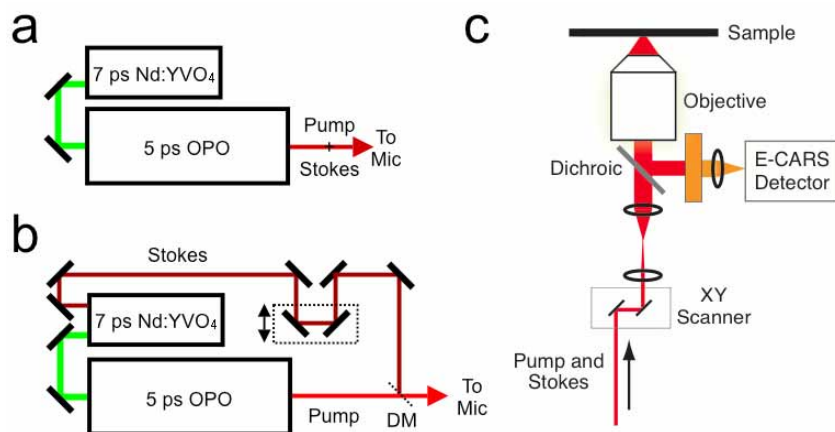

Fig. 1. Diagrams of the CARS microscopy system. (a) Laser configuration used to maximize the CARS imaging depth. The signal and idler pulse trains of the OPO exit collinearly and overlapped in time. (b) Laser configuration used to maximize the detected epi-CARS signal. The signal of the OPO is combined with the synchronized 1064 nm output of the Nd:VYO4 on a dichroic mirror (DM). A delay stage is used to overlap the two pulse trains in time. (c) Schematic of the CARS microscope. An inverted microscope was modified to use a nondescanned epi-detector to maximize the epi-CARS signal from the tissue.

2.3 Raman spectroscopy

Raman spectra of tissue slices were taken using a Raman microspectrometer (Labram, Horiba Jobin Yvon). Regions of the specimen were identified using reflected light microscopy. Spectra were collected using a long working distance 20X air objective (LWD C A20 PL, 0.4NA, Olympus) with the confocal pinhole fully opened in order to sample a large tissue volume. A 632 nm HeNe laser provided 5 mW of power at the laser focus. The spectra from healthy brain tissues were collected using a 100s integration time and were averaged twice. Spectra collected from diseased brain samples were integrated for 200s and averaged twice.

2.4 Animal handling

Severe combined immune deficiency (SCID) and double transgenic APP and PS1AD mice were acquired from Taconic Farm Inc. All mice were male. The SCID mice were imaged at the age of 6 weeks while the APP and PS1AD mice were imaged at 16 months of age. The APP and PS1AD mice imaged showed no evidence of plaque formation. All animals were maintained and housed according to the guideline of IAUAC and the standards of the Animal Research and Comparative Medicine committee of Brigham and Women's Hospital. To create a mouse model of a brain tumor, we injected human astrocytoma (a type of glioma) cells intracranially using a stereotactic system. Cells were cultured to subconfluence, trypsinized, washed twice in phosphate buffer solution (PBS), and resuspended ($5x10^7$/mL in 2 μl of PBS). 100,000 cells were injected into each mouse. Four weeks after the injection, the mice were sacrificed for brain harvest. After perfusion, the mouse brain was removed and kept in a 1% PBS solution prior to CARS imaging. Imaging sessions lasted no more than 90 minutes to keep the tissue section viable. 4% paraformaldehyde was used for fixation after each imaging session. Coronal sections of the mouse brain were acquired at approximately 2 mm posterior from the bregma. Each section had a thickness of 2 mm.

2.5 Imaging processing

In order to visualize the entire coronal brain slice, 20X, 700 x 700 μm CARS images were taken spanning the entire tissue sample using the motorized microscope stage. A median filter

was used to remove shot noise caused by the photomultiplier tube. A background image taken at a sample location outside the brain region was used to roughly compensate for the uneven brightness of individual images, and a moving average filter was used to remove background noise. The individual images were then divided by the background image, and a MATLAB® (MathWorks, Natick, MA) routine was used to stitch the individual images into a mosaic of the entire specimen.
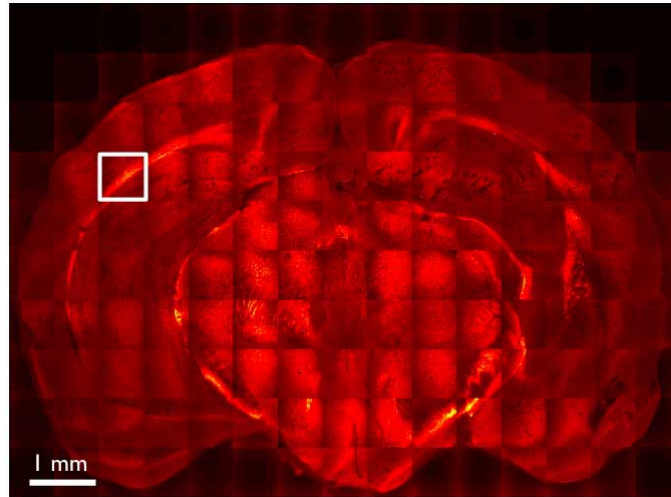

Fig. 2. Mosaic CARS microscopy image of a healthy APP and PS1AD mouse brain. Each single image is 700 x 700 μm in size. The brain slice was sectioned 2.8 mm posterior to the bregma. The single image enclosed by the white square is shown in Fig. 3. The pump and Stokes wavelengths were 816.7 and 1064 nm, respectively.

3. Results

3.1 Imaging large-scale brain structures

The 134-image, high-resolution mosaic CARS microscopy in Fig. 2 shows a coronal section from a healthy APP/PS1AD mouse brain. These images were produced by tuning into the 2845 cm^{-1} lipid CH$_2$ symmetric stretching mode. Brain myelin located in the oligodendrocyte sheaths coating the axonal bundles is rich in CH bonds, and thus the lipid CARS contrast produced intense CARS signal and excellent image contrast [16]. This section, taken 2.8 mm from the bregma, samples a wide range of brain structures containing both white and grey matter. Prominent white matter tracts that can be identified include the association fiber bundle in the centrum semiovale, the corpus callosum, and corticospinal tracts. Intense lipid band CARS signal arising from deep white matter tracts can be seen traversing the diencephalon and surrounding the deep brain nuclei. Fig. 3(a) shows a single 700 x 700 μm image of the margin of the corpus callosum, and illustrates the gray-white matter contrast, microstructural anatomy and cellular and tissue level resolution of these images. The ability to produce both intermediate spatial resolution images depicting gross anatomy and corresponding high resolution images from the same acquisition is a major advantage of this technique.
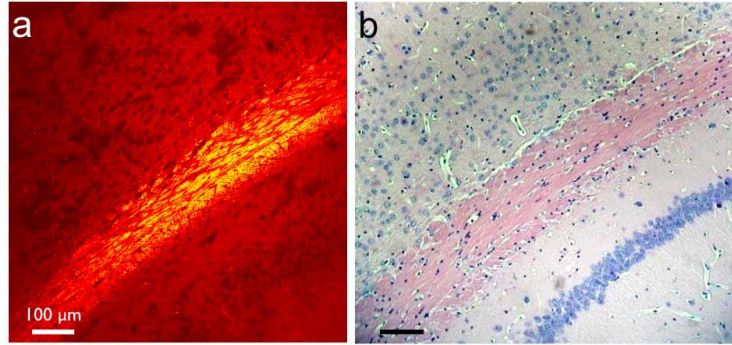
Fig. 3. (a). Single CARS image from Fig. 2. The pump and Stokes wavelengths were 816.7 and 1064 nm, respectively. (b) H&E image of the same region of the same mouse brain. Note the structures observable in both images, from upper left corner to the bottom right are the cortex, corpus callosum, oriens layer, and pyramidal layer.

As the signal strength in CARS images is due to the quadratic density of resonant vibrational modes, the observed contrast often differs significantly from familiar conventional histologic images. In order to validate the identification of structures in our CARS images with the histologic gold standard, tissue layers imaged with CARS were subsequently prepared and imaged using standard staining procedures. Figure 3(b) shows a 20X image of a haematoxylin and eosin (H&E) stained section taken at the same location approximately 50 μm deeper in the tissue from the CARS image in Fig. 3(a). The H&E stain is the most commonly used stain for medical diagnostics. The blue haematoxylin dye stains basophilic structures such as nuclei, while the pink eosin stains acidic cellular features such as proteins and fatty acids. The bright band in the CARS image [Fig. 3(a)] corresponds very well to the pink stained white matter bundle in the histological section. Dark regions in the CARS image at 2845 cm^{-1} are seen to correspond to the haemotaxylin-stained neuronal cell bodies. By comparing the contrast in the two images, the Oriens, Pyramidal, and CA1 layers of the hippocampus can also be identified in the CARS image, illustrating a level of cytoarchitectonic detail unattainable with conventional medical imaging techniques.
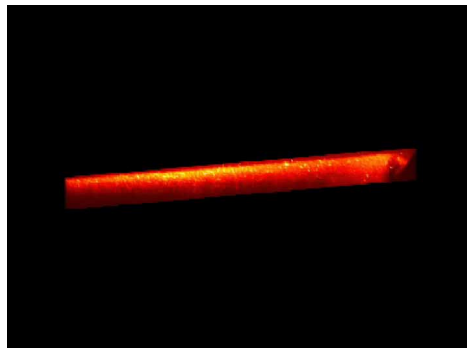

Fig. 4. (3.4 MB) Animation and three-dimensional reconstruction of a 50 μm depth stack in brain tissue taken with CARS microscopy. The first segment of the animation shows an uncorrected depth stack taken at 20x magnification in a coronal section containing the cortex (top) and white matter tracks streaming from the corpus collosum (bottom, not shown). At a depth of ~50 μm in the tissue, scattering from the white matter tracks has significantly decreased the CARS signal, while the CARS signal persists in the less scattering grey matter of the cortex. The second segment of the animation shows the three-dimensional reconstruction of the depth stack.

The maximum imaging depth was highly dependent on the wavelengths used and the local tissue environment. At the moderate laser powers used in this experiment (~100 mW), the 816.7 nm pump wavelength system was able to achieve a depth of approximately 50 μm in

grey matter, and 25 μm in the white matter corpus collosum (Fig. 4). The longer wavelength 920 nm pump system, on the other hand, was able to probe much deeper: 80 μm in grey matter such as the cortex and 40 μm deep in the corpus collosum. White matter tracks contain many axon bundles that strongly scatter light. While such scattering does increase the backscattered epi-CARS signal, it can significantly perturb the incoming pump and Stokes light. The highly scattering nature of brain tissue causes an enlargement of the pump and Stokes focal volumes, disrupts the overlap of the two foci, and leads to a reduction in laser focal power at the focus, causing the third-order CARS signal to degrade with depth. This imaging depth will be extended through adaptive approaches in the future [17-19].

3.2 Chemically-selective imaging

As a vibrational imaging technique, CARS microscopy has the capability to distinguish between structures based on their chemical compositions. Figure 5 shows three images of the same brain region in an APP/PS1AD mouse taken with CARS microscopy [Figs. 5(a) and (b)] and visualized using the H&E stain [Fig. 5(c)]. Figure 5(a) is a CARS image taken at the lipid CH_2 symmetric stretching frequency (2845 cm^{-1}) where the nonresonant background has been subtracted. The CARS signal arising from the myelinated axonal sheaths [16] radiating from the corpus callosum is here color coded in green to indicate positive CARS signal - signal greater than the nonresonant background. When the Raman shift is tuned away from the CH_2 stretch to the lipid "dipping" region at 2955 cm^{-1} [Fig. 5(b)], the image contrast changes dramatically: areas of previously positive CARS signal coded in green in Fig. 5(a) now show negative CARS signal, color coded in blue. This is explained by previous CARS spectroscopy studies [20-22], which demonstrate that CARS spectrum of lipids dips below the nonresonant background at 2955 cm^{-1} due to destructive interference with the nonresonant contribution.
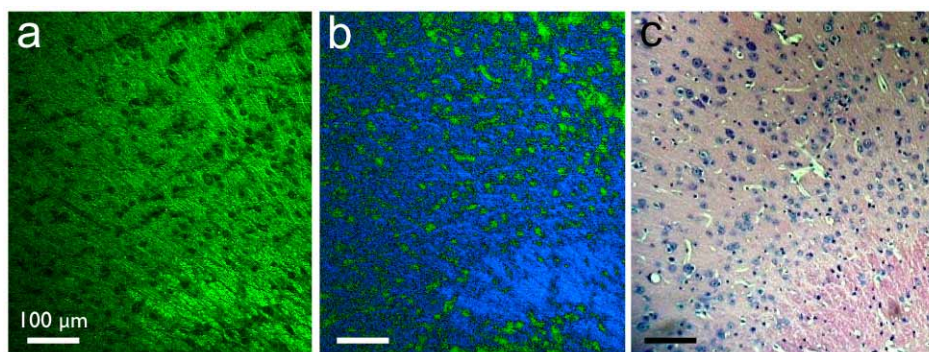

Fig. 5. Imaging the brain with chemical selectivity. All images were taken from the same brain used in the Fig. 2 mosaic. A nonresonant image was subtracted from (a) and (b). Regions of positive contrast (signal greater than the nonresonant background) are color coded green, while regions of negative contrast are color coded blue. (a) Positive lipid contrast image of CARS microscopy at 2845 cm^{-1}. (b) Negative lipid contrast image of CARS microscopy at 2955 cm^{-1} showing the cell bodies with positive contrast, (c) Corresponding H&E image. Neuronal cell bodies appear blue due to the haemotaxylin stain, while axons are dyed pink by eosin. The Stokes wavelength was 1064 nm.

Figure 5(b) also displays many small regions of positive (green) CARS signal that did not generate CARS signal at the CH_2 stretching frequency [Fig. 5(a)] and thus appeared black. These features correspond to neuronal cell bodies on the H&E section of the same tissue [Fig. 5(c)]. Previous Raman spectroscopy studies of brain tissue found that neuronal cells bodies have relatively low lipid content, explaining the low CARS signal at the CH_2 stretching frequency. By demonstrating that the substantial CH_3 stretch spectral density at 2920 cm^{-1} and 2960 cm^{-1} observed in neuronal cell bodies is associated with a large signal at the amide I vibrational band characteristic of protein, these same studies support that the neuronal cell body CH_3 stretch CARS signal arises from high protein content [23, 24]. Raman spectra

taken from the lipid-rich corpus callosum and high cell density hippocampal pyramidal layer of SCID mouse brain (Fig. 6) illustrate the differences in Raman band shape responsible for the positive neuronal cell body CARS signal in Fig. 5(b). The lower-energy lipid CH_2 bonds in axonal bundles give rise to a negative CARS signal at 2955 cm^{-1}, whereas the higher-energy protein CH_3 content in the cell bodies causes the CARS dip to occur at Raman shifts greater than 2955 cm^{-1}. This shift yields the positive CARS contrast observed for cell bodies in the 2950 cm^{-1} region.
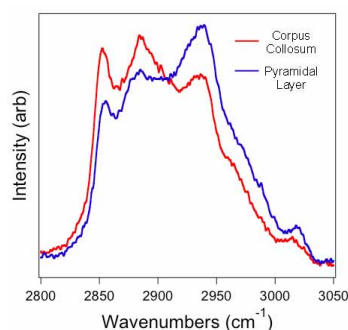
Fig. 6. Raman spectra acquired from fresh coronal slices of SCID mouse brain tissue immersed in PBS solution. The red line represents the Raman spectrum from the corpus collosum, while the blue line is the Raman spectrum from the nuclei-rich pyramidal layer of the hippocampus. Raman spectra were acquired in 100s and averaged twice.

The ability of CARS to provide such chemical selectivity allows for the reliable differentiation of cell body and axonal signatures, illustrating the potential of CARS microscopy for *in situ* imaging of unfixed brain tissues.
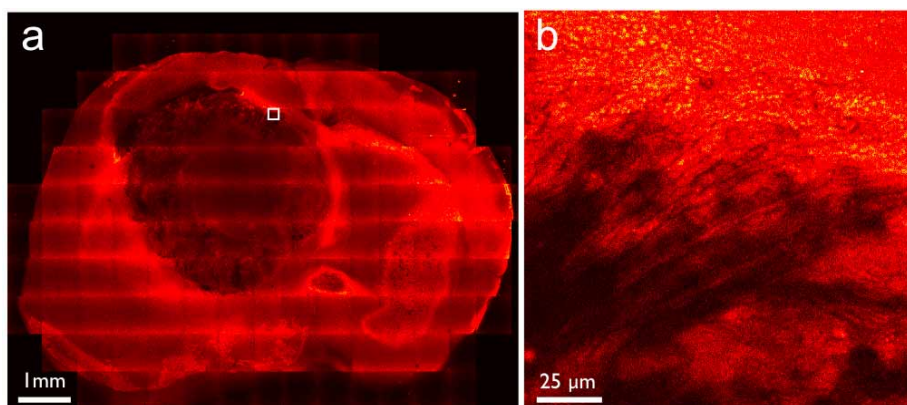

Fig. 7. CARS images of astrocytoma in a SCID mouse sacrificed 4 weeks after inoculation of tumor cells. The pump and Stokes wavelengths were 924.0 and 1254.2 nm, respectively. (a) A low resolution, large field of view mosaic CARS microscopy image provides chemically-selective anatomical information. Part (b) illustrates the ability of CARS to produce higher resolution images, in this case corresponding to the area enclosed by the rectangle in (a). This 80X, 175 x 175 μm image demonstrates the microscopic infiltration at the boundary between the tumor and normal tissue with a precision comparable to the conventional fixed tissue H&E histology images in Fig. 8.

3.3 Visualizing brain tumor margins

The chemically-selective contrast of CARS microscopy can be used to distinguish between healthy and diseased brain tissue. Figure 7(a) shows a full-brain mosaic of a SCID mouse

brain containing a human astrocytoma. The CARS image, taken at the CH$_2$ stretch to visualize lipid density, shows the extent of the tumor. The symmetry of the brain has been significantly altered by tumor growth with infiltration of the margin of the corpus callosum in the right hemisphere. Examining the tumor margin reveals the characteristic infiltration of normal white matter by invasive glioma [Fig. 7(b)]. In comparison, Fig. 8 shows an H&E microscopy image of a corresponding brain section from a different SCID mouse in the same group as the mouse imaged in Fig. 7. Comparison of this section with Fig. 7 reveals that the CARS image defines the tumor margin with comparable accuracy to the H&E stain. The tumor contrast in the CARS image arises from the destruction and displacement of normal white matter by the comparatively highly cellular and thus lipid deficient astrocytic glioma (Fig. 9). The low CARS signal level from the tumor made depth measurements difficult, though the penetration depth under these conditions is estimated to be ~50 µm when using a 920 nm pump and ~35 µm when using a 816.7 nm pump, based on literature tissue scattering parameters [25].
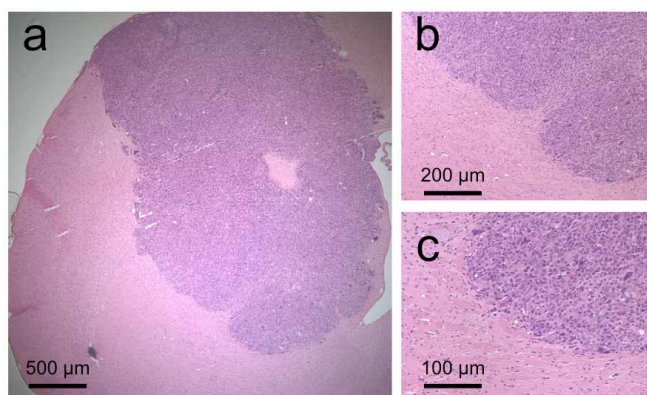

Fig. 8. H&E images of a brain tumor harvested from a different SCID mouse in the same group as the mouse imaged in Fig. 7. The brain slice was taken at approximately the same location as that of Fig. 7. (a) The boundary between the tumor and normal tissue at 4X, (b) 10X, and (c) 20X magnification.

4. Discussion

The 20X magnification, coronal section lipid band CARS images clearly depict major mouse brain white and gray matter structures, including the corpus callosum, layers of the hippocampus, the thalamus, and cingulum. In addition, the high sensitivity and chemical selectivity achievable by CARS without the use of labeling agents should allow far more specific tissue contrast specificity in the future. By tuning the Raman shift to image DNA, RNA, and protein bands it should be possible to overlay images acquired at different vibrational bands to produce composite images reflecting the complex molecular combination of brain tissue. While imaging at such bands is currently limited by a nonresonant electronic background in the CARS signal, technological improvements [11, 26] over the past few years have lead to a dramatic increase in the sensitivity and selectivity of CARS microscopy. In particular, Frequency-Modulation CARS (FM-CARS) microscopy [11] is especially promising for *in vivo* imaging. By rapidly toggling the Raman shift on and off a CARS resonance, FM-CARS suppresses the nonresonant background. In preliminary studies, this has increased sensitivity by three orders of magnitude, and new implementations of the technique currently underway promise further increases. Such improvements will enable future studies to determine the tumor detection sensitivity of CARS imaging systems.
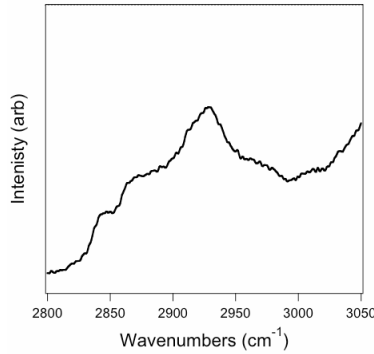
Fig. 9. Raman spectrum acquired from the center of a large astrocytoma in a fresh coronal slice of a SCID mouse brain tissue immersed in PBS. There is minimal Raman intensity at 2852 cm^{-1} and 2880 cm^{-1}, indicating the tissue is lipid deficient relative to normal brain tissue. The peaks at 2920 cm^{-1} and 2960 cm^{-1} arise due to the CH$_3$ symmetric and anti-symmetric stretching vibrations. The large signal increase after 3000 cm^{-1} is due to the water stretching vibration of PBS solution. The spectrum was integrated for 200s and averaged twice.

Potential clinical applications of CARS microscopy would initially complement and perhaps ultimately replace traditional histopathology. These may include minimally invasive microendoscopy for neuropathologic diagnosis of neoplastic and non-neoplastic brain diseases. Recent reports of *in vivo* optical microendoscopy in living mice have demonstrated that minimally invasive optical imaging of deep brain tissues can be performed through a fiber optic microendoscope [27, 28]. A CARS endoscope, based on similar miniaturized equipment, is technologically feasible and could be used to reduce or eliminate the need for brain tissue resection in definitive neurosurgical diagnosis of brain mass lesions [29]. A CARS-based microendoscope would also overcome any limitations in optical penetration depth. In addition to reducing the need for brain tissue biopsy *in situ,* CARS imaging may allow for more definitive diagnosis compared to the small fragmented samples obtained with needle biopsy, as images of intact tissue provide information about tissue architecture, vascularity, cellularity, inflammatory infiltration, mix of cell types and tissue invasion. This information, of great diagnostic significance in neuropathology, cannot be derived from the tissue samples obtained by current minimally invasive needle biopsy or suction extraction neurosurgical techniques. Moreover, because microendoscopy is minimally damaging to tissue, multiple samples could be acquired with greater safety than using current techniques, reducing the rate of non-diagnostic biopsies.

One example of an important neuropathologic problem that a CARS-based microendoscope could help to address would be the distinction of primary brain tumor from non-glial neoplasms, such as metastasis and lymphoma, and non-neoplastic mimics, such as infection, demyelination and ischemia. Differentiation of such tumor before resection of tissue would improve the safety and efficacy of definitive operative diagnosis of masses detected on conventional brain MRI. Furthermore, during definitive resection of glioma, CARS microendoscopy could be used to safely probe beyond the resection margin, allowing more complete tumor resection. Finally, in the neuropathology laboratory, CARS may also be able to augment traditional neuropathologic techniques by allowing non-destructive chemically specific analysis of small samples of excised tissue obtained at brain biopsy, as a complement to traditional light microscopy. This may improve the specificity of diagnosis and allow adequate tissue to be reserved for special stains and microarray analysis without the need for resection of larger tissue samples.

5. Conclusion

We demonstrate that CARS microscopy of fresh unfixed *ex vivo* mouse brain can be used to identify normal gray and white matter structures on several scales, to distinguish glioma from normal brain tissue, and to clearly identify the tumor margin. This data establishes the feasibility of CARS microscopy for tissue diagnosis of unstained brain tissue and provides the preliminary proof of principle needed to justify developing CARS-based techniques for imaging brain tissue *in vivo*. Although this dataset was intended only as a proof of principle, we found good agreements between the CARS microscopic images and H&E stained light microscopic images of the same specimen.

Acknowledgments

§These two authors contributed equally to this work